

Integrating Deflection Models and Image Feedback for Real-Time Flexible Needle Steering

Momen Abayazid, *Student Member, IEEE*, Roy J. Roesthuis, *Student Member, IEEE*,
Rob Reilink, *Student Member, IEEE*, and Sarthak Misra, *Member, IEEE*

Abstract—Needle insertion procedures are commonly used for diagnostic and therapeutic purposes. In this paper, an image-guided control system is developed to robotically steer flexible needles with an asymmetric tip. Knowledge about needle deflection is required for accurate steering. Two different models to predict needle deflection are presented. The first is a kinematics-based model, and the second model predicts needle deflection that is based on the mechanics of needle–tissue interaction. Both models predict deflection of needles that undergo multiple bends. The maximum targeting errors of the kinematics-based and the mechanics-based models for 110-mm insertion distance using a ϕ 0.5-mm needle are 0.8 and 1.7 mm, respectively. The kinematics-based model is used in the proposed image-guided control system. The control system accounts for target motion during the insertion procedure by detecting the target position in each image frame. Five experimental cases are presented to validate the real-time control system using both camera and ultrasound images as feedback. The experimental results show that the targeting errors of camera and ultrasound image-guided steering toward a moving target are 0.35 and 0.42 mm, respectively. The targeting accuracy of the algorithm is sufficient to reach the smallest lesions (ϕ 2 mm) that can be detected using the state-of-the-art ultrasound imaging systems.

Index Terms—Computer-assisted surgery, image-guided control, minimally invasive surgery, needle–tissue interactions, ultrasound.

I. INTRODUCTION

PERCUTANEOUS needle insertion is one of the most common minimally invasive surgical procedure. Needles are often used for diagnostic and therapeutic applications such as biopsy and brachytherapy, respectively. Clinical imaging techniques such as ultrasound and magnetic resonance images, and computed tomography scans are commonly used during needle insertion procedures to obtain the needle and target positions. Needles that are used in clinical procedures often have a bevel tip to easily cut and penetrate a soft tissue. Such needles naturally deflect from a straight path during insertion, which make them difficult to steer intuitively [1]. Moreover, the needles that

Manuscript received April 3, 2012; revised August 24, 2012; accepted November 19, 2012. Date of publication December 21, 2012; date of current version April 1, 2013. This paper was recommended for publication by Associate Editor J. Dai and Editor W. K. Chung upon evaluation of the reviewer's comments. This work was supported by funds from the Netherlands Organization for Scientific Research.

The authors are with the MIRA Institute for Biomedical Technology and Technical Medicine, University of Twente, 7522 NB Enschede, The Netherlands (e-mail: m.abayazid@utwente.nl; r.j.roesthuis@utwente.nl; r.reilink@utwente.nl; s.misra@utwente.nl).

This paper has supplementary downloadable material available at <http://ieeexplore.ieee.org>.

Color versions of one or more of the figures in this paper are available online at <http://ieeexplore.ieee.org>.

Digital Object Identifier 10.1109/TRO.2012.2230991

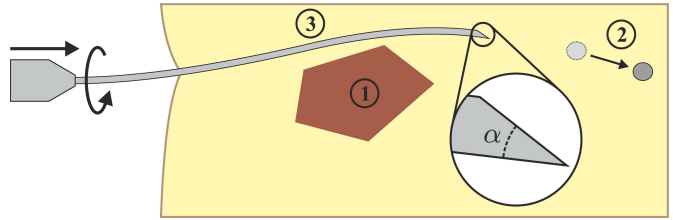


Fig. 1. Flexible needle with an asymmetric (bevel) tip can be used to steer around obstacles (1). Steering is accomplished by a combination of insertion and rotation at the base of the needle. Target motion (2) may occur during needle insertion, and this affects targeting accuracy. (3) Single needle rotation results in the needle having a *double-bend* shape. The bevel angle is denoted by α .

are used in surgical procedures are often thick and rigid. Such thick needles cause deformation of tissue, and this can result in target motion, which affects the targeting accuracy [2], [3]. Another disadvantage of using thick needles is that they cause patient trauma. Besides needle deflection and tissue deformation, other possible causes of targeting inaccuracy are patient motion during the procedure and physiological processes such as fluid flow and respiration. Inaccurate needle placement may result in misdiagnosis or unsuccessful treatment.

Thin needles were introduced to minimize patient discomfort [4]. Another advantage of using thin needles is that they are flexible and, therefore, facilitate curved needle paths. This enables steering the needle around obstacles (such as sensitive tissues) and to reach locations which are unreachable by rigid needles (see Fig. 1). Manually steering thin, flexible needles toward a desired location is challenging [5]. Using a robotic system which automatically steers the needle can assist the clinician. Such a system requires a model to predict the needle deflection to steer the needle to reach a certain location.

This paper presents two different models to predict needle deflection. The first is a kinematics-based model, which assumes that the needle tip follows a circular path. This model is based on the unicycle model that was presented by Webster *et al.* [6], but modifications are made to account for cutting tissue at an angle by bevel-tipped needles. The second model is a mechanics-based model which predicts deflection using needle–tissue interaction forces [7]. The mechanics-based model to predict deflection of needles undergoing multiple bends is presented in this study. Both models are validated using *double-bend* experiments (see Fig. 1).

In this study, image feedback is combined with the kinematics-based deflection model to steer the needle toward a target. Charge-coupled device (CCD) camera images are used for image feedback in the first set of experiments to evaluate

the tracking and steering algorithms. Experiments are then performed using ultrasound images to demonstrate that the presented framework is applicable to a clinical imaging modality. To the best of our knowledge, the use of ultrasound images to steer a bevel-tipped flexible needle ($\phi 0.5$ mm diameter) toward a moving target (less than 2 mm diameter) has not been investigated. The study also provides a method that allows the needle to move along a certain path using set points during the insertion into a soft-tissue phantom. The elasticity of the phantom affects the needle deflection [8], [9]. An acoustic radiation force impulse (ARFI) technique is an ultrasound-based noninvasive method that is used to measure the elasticity of the soft-tissue phantom.

This paper is organized as follows: Section II presents the related work in the area of flexible needle steering. Section III describes the needle deflection models and the experimental setup used for model validation. Section IV presents the control system that is used to steering the needle during insertion and the image processing techniques that are used for feedback. In Section V, the experimental results are presented, followed by Section VI, which concludes and provides directions for future work.

II. RELATED WORK

In the recent years, several research groups have developed algorithms for image-guided needle steering. Some of these algorithms encompass needle deflection models (see Section II-A), and techniques to track the needle tip and target in real time (see Section II-B). In this section, algorithms that were used in previous studies are discussed. The section also concludes by briefly presenting our proposed method for needle steering.

DiMaio and Salcudean [10] were among the first to investigate steering needles through a soft tissue. They developed a needle Jacobian which relates needle base motion outside the tissue to needle tip motion inside the tissue. Maneuvering the needle base causes the soft tissue around the needle to deform, and this enabled them to place the needle tip at a desired location. Glozman and Shoham [5] also used base maneuvering to steer the needle. A model was used to simulate the interaction between a needle and a soft tissue. Needle steering was accomplished by solving the forward and inverse kinematics of this model. Neither DiMaio and Salcudean [10] nor Glozman and Shoham [5] used needles with an asymmetric tip. The advantage of using needles with asymmetric tips is that the needle deflection can be used for steering. The direction of deflection (in the planar case) is changed by rotating the needle 180° during insertion (see Fig. 1). Several research groups have focused on the steering of flexible needles with a bevel tip, e.g., [1], [6], [11]–[18]. The deflection of a needle with a bevel tip can also be controlled using duty cycle rotation [19].

A. Needle Deflection Models

Webster *et al.* [6] presented an approach in which they used the kinematics of unicycle and bicycle models to predict the needle deflection. In their work, they assumed that the needle tip moves along a circular path. The unicycle model assumed

that the paths followed by the needle before and after rotation are tangent to each other. In the bicycle model, the paths before and after rotation are not assumed to be tangent to each other. They assumed relatively stiff tissue and showed that their model agrees with experiments. The kinematics-based model by Webster *et al.* is limited since it did not account for needle–tissue interaction along the length of the needle.

Several groups focused on a mechanics-based approach to model needle deflection. They used the interaction between the needle and surrounding tissue to predict the needle curvature. Alterovitz *et al.* [12] presented a planning algorithm for a needle with a bevel tip to determine the insertion point in order to reach a desired target. Finite-element (FE) modeling was used to model the needle–tissue interaction, and this was employed in their planner to account for soft-tissue deformation. FE modeling requires computing power that is not convenient to implement in real-time control. Therefore, analytical needle deflection models were proposed to predict the deflection of needles with a bevel tip during insertion in a soft tissue [9], [13], [20], [21].

Kataoka *et al.* [20] presented a force-deflection model, where they assumed a constant force per unit needle length. This assumption resulted in discrepancies with the experimental deflection. Abolhassani and Patel [13] described a model that related force/torque data at the needle base to deflection. They did not account for tissue deformation along the needle shaft. This led to errors between measured and predicted deflections. Misra *et al.* [21] presented a mechanics-based model that predicted needle deflection using the Rayleigh–Ritz formulation. Roesthuis *et al.* [9] extended this model by adding spring supports along the needle shaft. However, none of these models could predict the needle deflection for the case when the needle is rotated during insertion (i.e., multiple bends). The authors presented a mechanics-based model to predict deflection of a needle undergoing multiple bends [7]. In addition to the mechanics-based model, a modification of the unicycle model is presented in this study. This model requires fewer parameters than the bicycle model to describe needle deflection accurately. This kinematics-based model is compared with the mechanics-based model. The deflection model and real-time needle tracking are used to develop a feedback control system to steer flexible needles.

B. Needle and Target Tracking

In previous studies, a needle (without a bevel tip) and target positions were tracked in fluoroscopic and ultrasound images using image processing algorithms [5], [22]. In ultrasound images, the needle visibility is affected by the operator's skill in aligning the needle in the ultrasound imaging plane [22], [23]. Okazawa *et al.* [24] developed two algorithms that were based on the Hough transform to detect the needle shape in ultrasound images during insertion. There are other segmentation techniques that can be used for needle tracking based on corner detection and subtraction [22], [25]. The main advantage of the subtraction and corner detection techniques is that the required processing time is short, which makes these techniques suitable for real-time applications. The disadvantage of using the

subtraction method is that it is sensitive to motion of a soft tissue. Corner detection is immune to such artifacts that may appear in the image outside the processed region. Magnetic tracking sensors [26], [27] and fiber optic strain sensors [28] were also used for real-time needle tracking. Tracking the needle tip slope and the target position is also required to steer the needle. The tip slope changes during insertion due to needle deflection. Target displacements over 2.0 mm have been measured during placement of a biopsy needle in the breast [2], [29]. Target displacement introduces targeting errors [3]. The target position needs to be measured in each frame in order to increase the targeting accuracy of the steering algorithm.

C. Proposed Algorithm for Steering

In this study, two different (kinematics-based and mechanics-based) needle deflection models are presented. A revised set of experiments are performed to compare the results of the models. The kinematics-based model is used in the proposed control system. The system uses processed images for feedback control. A real-time needle tracking algorithm is developed based on processing camera and ultrasound images. The Harris corner detection technique is used for tracking the needle ($\phi 0.5$ mm) tip position. The algorithm that is used to measure the tip slope is based on image moments [30], [31]. The displacement of the target is detected to reduce the targeting error. Target motion is measured by calculating the centroid of the target shape using image moments [32]. The tracked moving target is of $\phi 2.0$ mm. The proposed algorithms for needle and target motion tracking are applicable for both CCD camera and ultrasound images. The tracking algorithms are suitable for real-time applications. The steering algorithm uses set points to specify a certain path for the needle to follow during insertion. In the control system, it is assumed that the needle follows a circular path during insertion. This assumption was used in previous studies [6], [12]. Deviation of the needle from its planned path due to disturbances or inaccurate assumptions is corrected in real time by the developed algorithm.

III. NEEDLE DEFLECTION MODELS

In this section, two models to predict needle deflection are presented. Both models assume that the needle bends in plane (2-D). The first model uses a kinematics-based approach, while the second model is based on the mechanics of needle–tissue interaction. Both models assume that the needle shaft follows the path that is described by the needle tip. The experimental setup and the soft-tissue phantom used are described. Experiments are presented to fit the parameters of both models. Experiments are performed to validate both models in the case of steering toward a target with a single rotation.

A. Kinematics-Based Model

The idea of using nonholonomic kinematics to describe the needle path of a flexible, bevel-tipped needle has been demonstrated by Webster *et al.* [6]. The approach assumes that the needle tip follows a circular path. They proposed using a uni-

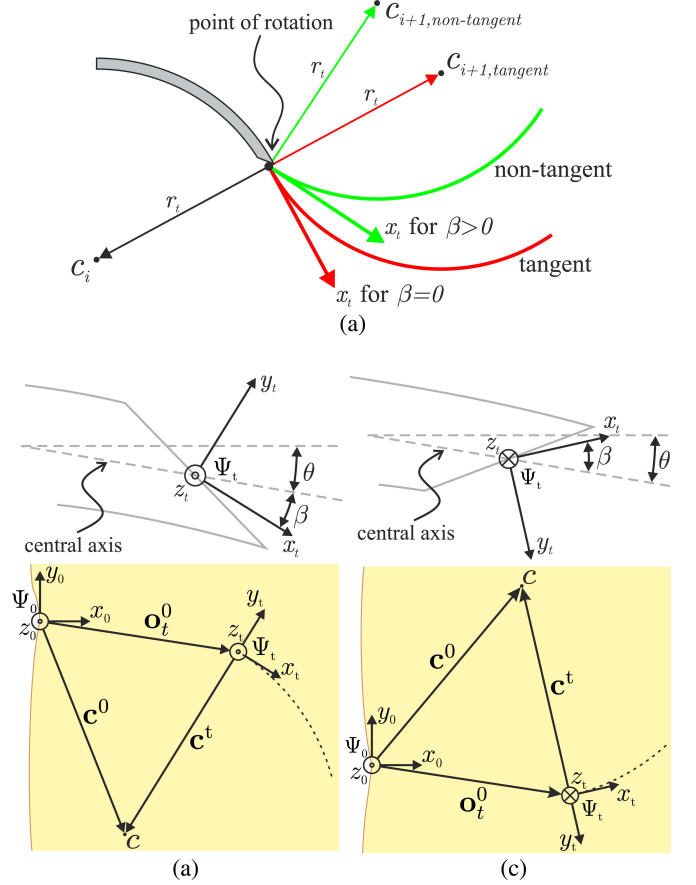


Fig. 2. Kinematics-based approach to describe the needle path: The needle travels in the direction of x_t along a circular path with centre c and radius r_t . (a) Effect of the cut angle β is shown: the resulting needle path after needle rotation for a tangent needle path ($\beta = 0$) and a nontangent needle path ($\beta > 0$). (b) Frame (Ψ_t) is rigidly attached to the needle tip, and the cut angle is modeled by rotating the frame by the cut angle with respect to the central axis of the needle. A needle bevel tip is facing up, which causes the needle to deflect downward. (c) Needle rotation is performed, indicated by a rotation of the tip frame around the central axis of the needle. This results in the needle to deflect upward.

cycle model with a steering constraint to describe the circular needle path. The unicycle model could not describe the needle path when needle rotation is performed during insertion. This is due to the fact that the circles describing the needle path before and after needle rotation are not tangent to each other [see Fig. 2(a)]. To describe the nontangent needle path, the bicycle method is used.

In this study, a modification of the kinematics-based unicycle model is presented, which accounts for the nontangent needle path (see Fig. 2). It has been observed that a bevel-tipped needle cuts the tissue at an angle from the central axis of the needle [12], [21]. We denote this angle as the cut angle β . The cut angle is modeled by placing a frame at the needle tip (Ψ_t), which is rotated by the cut angle with respect to the central axis of the needle [see Fig. 2(b)]. The needle tip travels through a soft tissue in the direction that is indicated by x_t . Rotation of the needle around its central axis results in a change of direction of x_t [see Fig. 2(c)]. This causes the needle tip to follow a path which is not tangent to its path before rotation [see Fig. 2(a)]. The

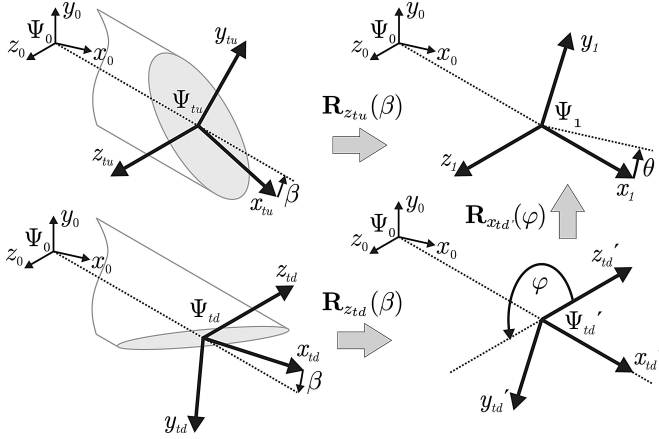


Fig. 3. (Top left) Needle tip when bevel face is pointed up (Ψ_{tu}). (Bottom left) Needle tip when bevel face is pointing down (Ψ_{td}). The rotations are shown to align tip frames (Ψ_{tu} and Ψ_{td}) with the global coordinate frame (Ψ_0). The final rotation \mathbf{R}_1^0 is not shown.

needle tip follows the circumference of a circle (center c and radius r_t) as shown in Fig. 2(a). The needle tip lies at the origin of frame Ψ_t ; expressed in the global coordinate frame this becomes $\mathbf{o}_t^0 = [x_{tip} \ y_{tip} \ z_{tip}]^T$. Since planar needle deflection in the x_0y_0 -plane is assumed, z_{tip} equals zero. The needle deflection y_{tip} can be expressed as a function of the needle tip x -coordinate x_t

$$y_{tip} = c_y^0 \pm \sqrt{r_t^2 - (x_{tip} - c_x^0)^2} \quad (1)$$

where c_x^0 and c_y^0 are the x - and y -coordinates of the circle centre expressed in the global coordinate frame (Ψ_0), respectively. The circle centre coordinates \mathbf{c}^0 that are expressed in the global coordinate frame are calculated by performing a homogeneous transformation

$$\mathbf{c}^0 = \mathbf{H}_t^0 \mathbf{c}^t \quad (2)$$

where \mathbf{c}^t are the homogeneous coordinates of the circle centre expressed in the tip frame

$$\mathbf{c}^t = [c_x^t \ c_y^t \ c_z^t \ 1]^T = [0 \ -r_t \ 0 \ 1]^T. \quad (3)$$

In (2), \mathbf{H}_t^0 represents the homogeneous transformation from the tip coordinate frame to the global coordinate frame

$$\mathbf{H}_t^0 = \begin{bmatrix} \mathbf{R}_t^0 & \mathbf{o}_t^0 \\ \mathbf{0}_3^T & 1 \end{bmatrix}. \quad (4)$$

The rotation matrix \mathbf{R}_t^0 depends on the orientation of the bevel tip (see Fig. 3). In the case of the bevel face pointing up, the tip frame (Ψ_{tu}) needs to be rotated by the cut angle about the z_{tu} -axis to align it with the central axis of the needle

$$\mathbf{R}_{tu}^1 = \mathbf{R}_{z_{tu}}(\beta). \quad (5)$$

If the bevel face is pointed down, the frame Ψ_{td} first needs to be rotated about the z_{td} -axis by the cut angle, then a rotation of φ about the x_{td}' -axis is required to align it with the central axis of the needle

$$\mathbf{R}_{td}^1 = \mathbf{R}_{z_{td}}(\beta) \mathbf{R}_{x_{td}'}(\varphi). \quad (6)$$

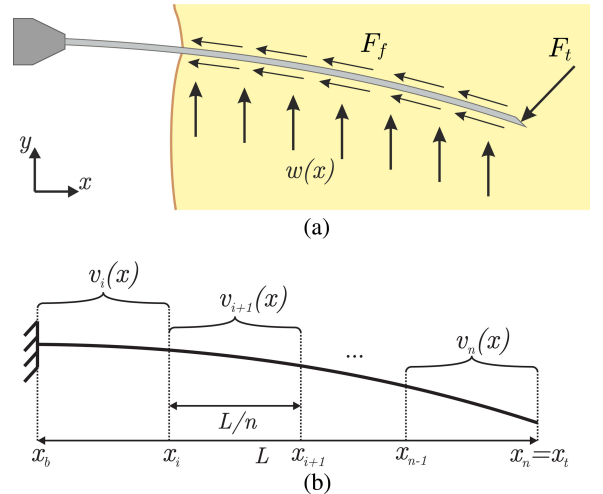


Fig. 4. (a) As a flexible needle with a bevel tip is inserted into soft tissue, it is subject to needle–tissue interaction forces. (b) The needle is modeled as a cantilever beam. The needle is divided into n elements each described by its own shape function [$v_i(x)$].

Finally, a rotation equal to the needle tip slope θ around the z_1 -axis has to be performed to align the x_1 -axis with the x_0 -axis

$$\mathbf{R}_1^0 = \mathbf{R}_{z_1}(\theta). \quad (7)$$

Thus, for the bevel face pointing up, \mathbf{R}_t^0 in (4) is calculated by

$$\mathbf{R}_t^0 = \mathbf{R}_{tu}^0 = \mathbf{R}_1^0 \mathbf{R}_{tu}^1 \quad (8)$$

and for the bevel face pointing down this is

$$\mathbf{R}_t^0 = \mathbf{R}_{td}^0 = \mathbf{R}_1^0 \mathbf{R}_{td}^1. \quad (9)$$

Using (2)–(9), needle tip position (x_{tip}, y_{tip}) , and needle tip slope θ , the centre of the circle c_{i+1} that describes the next needle path can be determined at each instant during insertion. This allows predicting the future needle path if a rotation is to be made. This is essential to steer the needle, which will be discussed in later sections.

B. Mechanics-Based Model

A needle is subjected to needle–tissue interaction forces when it is inserted into a soft tissue [see Fig. 4(a)]. When the needle travels through the tissue, force is required to cut the tissue and create a path through the tissue. This is modeled by a force at the tip of the needle F_t . If the needle has an asymmetric tip, the forces at the needle tip have an uneven distribution, causing the needle to deflect from a straight insertion path [21]. In the case of a bevel-tipped needle, the tip force is considered to act normal to the bevel face. When the needle travels through the tissue, friction acts on the needle shaft. This is modeled by a force F_f acting tangent to the needle shaft. As the needle is inserted, it is supported by the surrounding tissue. The force exerted by the tissue surrounding the needle (i.e., an elastic support) is modeled as a distributed load ($w(x)$) along the inserted part of the needle.

The needle is modeled as a cantilever beam [see Fig. 4(b)]. Assuming small needle deflections, only transversal needle deflection is considered. The needle is stiff in the axial direction,

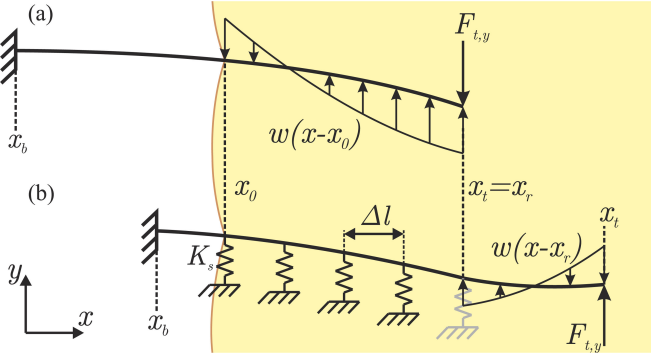


Fig. 5. (a) Needle deflects due to a combination of needle tip force $F_{t,y}$ and distributed load $w(x)$. (b) As the needle is rotated at x_r , the orientation of tip force and distributed load change. This causes the needle to deflect in the opposite direction. In order to model the *double-bend* shape, the part of the needle prior to rotation ($x_0 \leq x \leq x_r$) is fixed by a series of springs.

and hence, shortening of the needle is not considered. When the needle is inserted without being rotated, it has a *single-bend* shape [see Fig. 5(a)]. The needle deflects due to a combination of the distributed load and the tip force. Needle rotation is performed when the insertion distance equals the rotation distance ($x_t = x_r$). This results in a change of orientation of the bevel tip, and hence, the tip force also changes direction [see Fig. 5(b)]. This causes the needle to deflect in the opposite direction. For a single rotation, this results in the needle having a *double-bend* shape. To model this, the part of the needle before rotation is fixed by a series of springs. Given a sufficiently small spring spacing Δl , one can approximate an elastic foundation [33]. The stiffness of such an elastic foundation K_t is described in terms of stiffness per unit length and depends on needle and tissue properties. The length of the foundation in Fig. 5(b) equals $x_r - x_0$, resulting in a foundation stiffness K_t of

$$K_t = K_0(x_r - x_0). \quad (10)$$

For a total number of m springs, this results in a spring stiffness K_s of $\frac{K_t}{m}$. The distributed load is applied to the part after rotation and this enables modeling of a needle undergoing multiple bends.

To evaluate the deflected needle shape ($v(x)$) under the action of distributed load and tip force, the Rayleigh–Ritz method is used. Rayleigh–Ritz is a variational method in which equilibrium of the system is established using the principle of minimum potential energy [34]. For a mechanical system, the total potential energy is expressed as

$$\Pi = U - W \quad (11)$$

where U represents the energy that is stored in the system, and W is the work done on the system by external forces. To find the deflected needle shape using the Rayleigh–Ritz method, an assumed displacement (shape) function has to be defined. Several shape functions were evaluated, and it is found that a cubic function is a suitable shape function

$$v(x) = a_0 + a_1 x + a_2 x^2 + a_3 x^3. \quad (12)$$

For complex needle shapes, a single shape function as in (12) is not sufficient to approximate the deflected needle shape. Therefore, the needle is divided [see Fig. 4(b)] into a number of elements n , each described by their own shape function ($v_i(x)$)

$$v(x) = \begin{cases} v_i(x), & x_{i-1} \leq x \leq x_i \\ v_{i+1}(x), & x_i \leq x \leq x_{i+1} \\ \vdots & \vdots \\ v_n(x), & x_{n-1} \leq x \leq x_n \end{cases} \quad (13)$$

where

$$v_i(x) = a_{0,i} + a_{1,i}x + a_{2,i}x^2 + a_{3,i}x^3. \quad (14)$$

The unknown coefficients $a_{0,i}, \dots, a_{3,i}$ are determined using the Rayleigh–Ritz method.

For the first needle element ($i = 1$), x_{i-1} equals x_b , and for the last element ($i = n$), x_i equals x_t . Each of the shape functions has to satisfy the geometric boundary conditions of the system. Since the needle is fixed at the base, the needle slope $\theta(x)$ and deflection $v(x)$ are zero at the base

$$v_1(x_b) = 0 \text{ and } \theta_1(x_b) = \frac{dv_1}{dx}|_{x=x_b} = 0. \quad (15)$$

Furthermore, the shape functions have to satisfy continuity conditions, meaning constant deflection and needle slope at the boundaries of the elements

$$v_i(x_i) = v_{i+1}(x_i) \text{ and } \theta_i(x_i) = \theta_{i+1}(x_i). \quad (16)$$

For the *single-bend* case [see Fig. 5(a)], the stored energy equals the strain energy due to transversal needle bending ($U = U_b$). Using Euler–Bernoulli beam theory [35], the strain energy due to transversal bending U_b is found to be

$$U_b = \frac{EI}{2} \int_{x_b}^{x_t} \frac{d^2 v(x)}{dx^2} dx \quad (17)$$

where E and I represent the Young's modulus and second moment of inertia of the needle, respectively. The needle is cylindrical and EI is constant along the length of the needle.

For a needle undergoing multiple bends, energy is also stored in the springs [see Fig. 5(b)]. The stored energy is the sum of the energy due to needle bending as defined in (17) and the spring energy for a total number of m springs

$$U_s = \sum_{k=0}^m \frac{1}{2} K_s v(x_k)^2 \quad (18)$$

where K_s represents the spring stiffness, and $v(x_k)$ is the amount of deflection for the k th spring with respect to the bend configuration, as shown in Fig. 5(b). The work done on the system by external forces is the sum of the work done by the distributed load W_d and concentrated tip load W_c :

$$W = W_d + W_c. \quad (19)$$

The work done by the distributed load is given by

$$W_d = \int_{x_0}^{x_t} w(x)v(x)dx \quad (20)$$

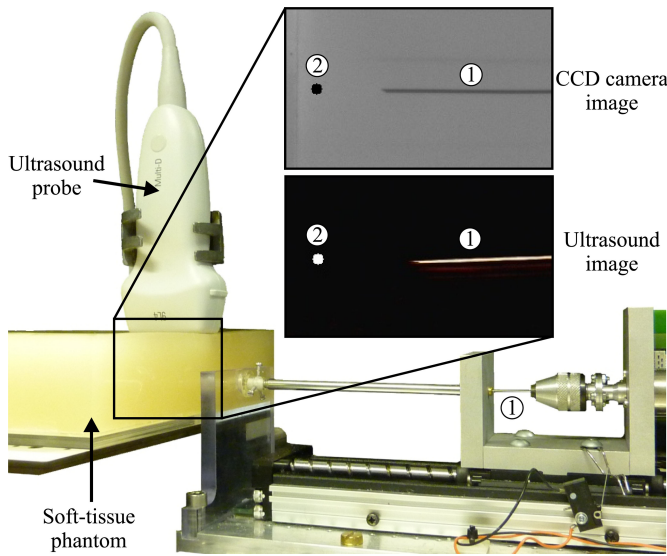


Fig. 6. Needle steering setup. A linear stage is used to insert the Nitinol needle (1) into a soft-tissue phantom and steer it toward a target (2). Needle and target tracking is done using a CCD camera and ultrasound images. Steering can be performed either using a CCD camera or ultrasound images.

and the work done by concentrated tip load is given by

$$W_c = F_{t,y} v(x_t) \quad (21)$$

where $v(x_t)$ is the deflection at the needle tip.

The shape functions defined in (14) are substituted in the equations for the stored energy [see (17) and (18)] and work [see (20) and (21)]. This results in the total potential energy of the system, defined in (11), to be a function of the shape functions, and hence the unknown coefficients

$$\Pi = f(v_i(x)) = f(a_{0,i}, a_{1,i}, a_{2,i}, a_{3,i}). \quad (22)$$

The equilibrium of the system is found by taking the partial derivative of the total potential energy with respect to each of the shape functions' unknown coefficients

$$\frac{\partial \Pi}{\partial a_{k,i}} = 0 \quad (23)$$

for $k = 0, 1, 2, 3$ and $i = 1, \dots, n$. The unknown coefficients $a_{k,i}$ are calculated by solving the system of equations obtained in (23). Substitution of the coefficients back into (13) and (14) gives the deflected needle shape.

Experimental data are used to evaluate the parameters for both needle deflection models. These parameters are the radius of curvature and the cut angle for the kinematics-based model and the distributed load for the mechanics-based model. In the next sections, the experimental setup is first introduced, and then experiments are presented which are used to evaluate the parameters. With the parameters known, both models are then validated in a series of (open-loop) steering experiments.

C. Experimental Setup

The experimental setup used to insert needles into soft-tissue phantoms is shown in Fig. 6 [9]. The setup has two degrees of freedom: translation along and rotation about the insertion axis

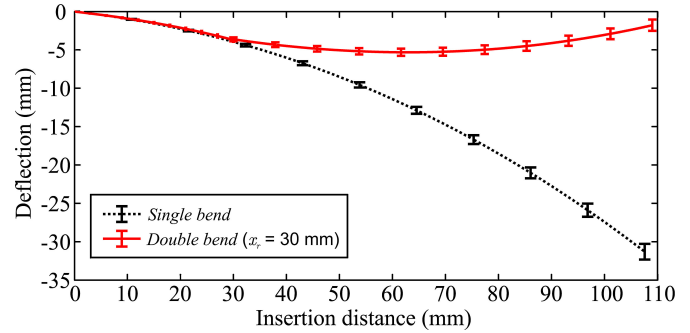


Fig. 7. Experimental needle tip deflection (mean) for the *single-bend* and the *double-bend* case (x_r is the distance at which rotation is performed). In both cases, five insertions are performed, and the standard deviation σ is shown by the error bars. The mean final tip deflection is -31.3 mm ($\sigma = 1.0$ mm) and -1.8 mm ($\sigma = 0.7$ mm) for the *single-bend* and *double-bend* case, respectively. The curves show the tracked needle tip positions during insertion.

for steering. A Sony XCDSX90 CCD FireWire camera (Sony Corporation, Tokyo, Japan) is mounted 450 mm above the setup and is used for imaging. For ultrasound imaging, a Siemens ACUSON S2000 (Siemens Healthcare, Mountain View CA) is used.

The needle is made of Nitinol wire ($\phi 0.5$ mm). Nitinol is a nickel-titanium alloy which, at a certain temperature range, has the property of being superelastic. This means the needle can undergo very large elastic deformations, without plastically deforming, allowing it to return to its initial (straight) shape. Nitinol ($E = 75$ GPa) is also more flexible than steel ($E = 200$ GPa); this increases the deflection and, hence, improves the steering capabilities of the needle. The needle tip is polished to a bevel angle α of 30° . Gelatin is used as a soft-tissue phantom. Gelatin phantoms are made by mixing gelatin powder (Dr. Oetker, Bielefeld, Germany) with water at a temperature of 40°C . The mixture is then put in a plastic container ($170 \times 30 \times 200$ mm 3). The gel solidifies after 5 h at a temperature of 7°C . For a gelatin-to-water mixture (by weight) of 14.9%, the elasticity is found to be 35.5 kPa. This elasticity is similar to what is found in breast tissue [36]. The elasticity is determined in a uniaxial compression test using the Anton Paar Physica MCR501 (Anton Paar GmbH, Graz, Austria). van Veen *et al.* [8] investigated the effect of several system parameters on needle deflection including soft-tissue phantom elasticity. Each needle insertion is done at a new location in the soft-tissue phantom to avoid influence of previous insertions on the current experiment.

D. Model Fitting

As mentioned in Section III-B, experimental data are used to evaluate the parameters for both models. The kinematics-based model requires the cut angle and the radius of curvature, and the mechanics-based model requires the distributed load. To evaluate these parameters, both *single-bend* and *double-bend* experiments are performed. In all experiments, the Nitinol needle is inserted a total distance of 110 mm in the soft-tissue phantom at a speed of 5 mm/s. The insertion speed is chosen to be within the range of speeds that are used in clinical applications (0.4–10 mm/s) [37]. In the *double-bend* experiment, a 180° rotation

TABLE I
RESULTS OF STEERING THE NEEDLE TOWARD A TARGET AT TWO DIFFERENT LOCATIONS (y_T) USING THE KINEMATICS-BASED AND THE MECHANICS-BASED MODELS

Model	y_T (mm)	x_r (mm)	$y_{tip,exp}$ (mm)	$e(x_T)$ (mm)	$\sigma(x_T)$ (mm)
Kinematics	-10.0	44.2	-10.8	0.8	0.4
	-20.0	64.2	-20.6	0.6	0.5
Mechanics	-10.0	42.8	-10.4	0.4	0.5
	-20.0	62.8	-18.3	1.7	0.2

Note: rotation distance x_r , experimental tip deflection ($y_{tip,exp}$), tip error e_{x_T} , and the standard deviation of final tip deflection $\sigma(x_T)$.

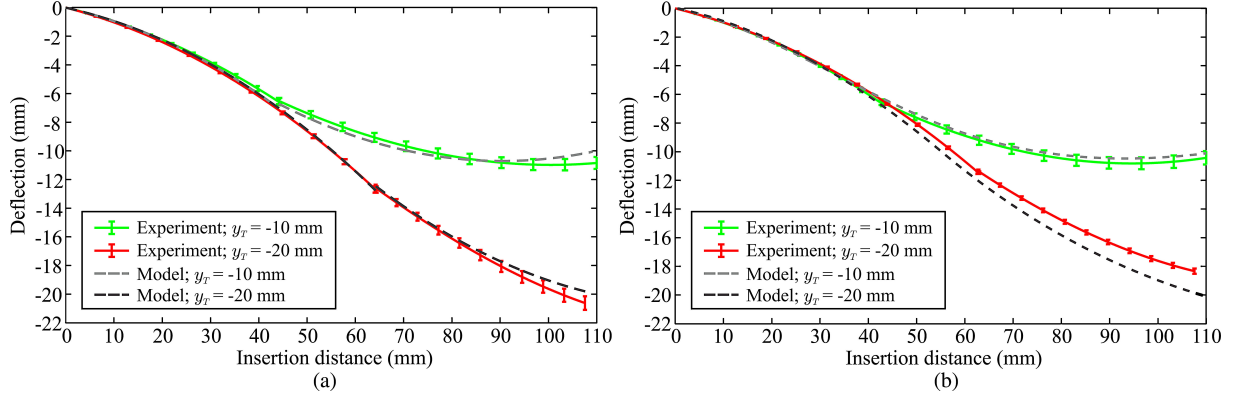


Fig. 8. Both needle deflection models are used to steer the needle toward two different target locations ($y_T = -10$ mm and $y_T = -20$ mm): (a) kinematics-based model and (b) mechanics-based model. For each experiment, a total of five insertions are performed. The results of the experiments shown here are presented in Table I.

is performed at an insertion distance x_r of 30 mm. The needle tip is tracked during the experiment, and the resulting needle tip deflection is shown in Fig. 7.

In order to evaluate the radius of curvature r_t for the kinematics-based model, a circle is fitted to the deflection of the *single-bend* experiment. This fitting is done in a least squares sense using a method described by Pratt [38]. The result of this fitting, for a total of five insertions, is a circle with a radius of curvature of 270.5 mm (standard deviation $\sigma = 5.7$ mm). The cut angle β is determined by fitting the path after needle rotation to the experimental deflection of the *double-bend* case. This results in a cut angle of 2.0°.

The distributed load ($w(x)$) for the mechanics-based model is evaluated by minimizing the difference between experimental deflection ($v_{exp}(x)$) and simulated deflection ($v_{sim}(x)$). The criterion used for fitting is a combination of error along the needle shaft ε_1 and error at the needle tip ε_2

$$\varepsilon = \varepsilon_1 + \varepsilon_2 \quad (24)$$

where

$$\varepsilon_1 = \int_{x_0}^{x_t} (v_{exp}(x) - v_{sim}(x))^2 dx \quad (25)$$

and

$$\varepsilon_2 = (v_{exp}(x_t) - v_{sim}(x_t))^2. \quad (26)$$

Several load profiles were evaluated for the distributed load (e.g., constant, linear, triangular), but the best fit was found using a

cubic load profile

$$w(x) = b_0 + b_1 x + b_2 x^2 + b_3 x^3. \quad (27)$$

Further, using a cubic load profile for the distributed load agrees with the assumption that the tissue acts as an elastic support for the needle as it bends. The assumed load profile is substituted in (20) and then the resulting needle deflection ($v_{sim}(x)$) is evaluated using the Rayleigh–Ritz method. The coefficients (b_0, \dots, b_3) are determined by minimizing (24).

Besides the distributed load, the mechanics-based model also requires the tip force F_t and the stiffness of the elastic foundation per unit length K_0 . The tip force depends on the geometric properties of the needle and tissue elasticity, as already shown in other studies [1], [9], [21]. In [9], the tip force was determined to be 0.4 N for a ϕ 1.0-mm needle with a 30° bevel angle. It was also observed that the tip force is almost constant during insertion. Misra *et al.* [21] showed that the magnitude of the tip force is proportional to the bevel surface area. Therefore, for the ϕ 0.5-mm needle that was used in this study, a constant tip force of 0.1 N is assumed ($\frac{0.5^2}{1.0^2} \times 0.4 = 0.1$). The stiffness of the elastic foundation per unit length also depends on the geometric properties of the needle and tissue elasticity. The stiffness is calculated such that the difference between model-predicted deflection and experimental data is minimized. The best fit with experimental deflection is found for $K_0 = 0.1$ N/mm². When using different needle–tissue combinations, this value is expected to change.

With the parameters evaluated for both models, it is now possible to predict needle deflection. In the next section, both

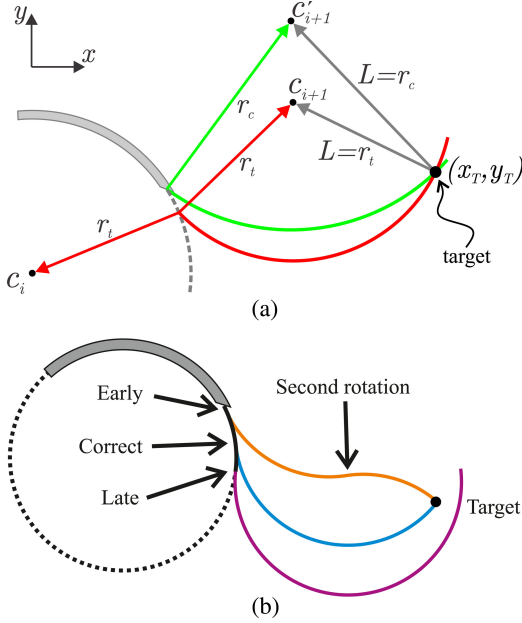


Fig. 9. (a) Variation in experimental conditions between insertions causes change in the radius of curvature of the needle r_t . Choosing the control radius r_c larger than the expected needle radius of curvature r_t results in an early rotation around the center c'_{i+1} . (b) Early needle rotation is corrected by performing additional rotations (orange). No additional rotation is required if the needle rotates at the correct instance (blue). If needle rotation is done late, then the target cannot be reached by performing additional rotations (purple).

models will be validated by performing open-loop steering experiments.

E. Open-Loop Needle Steering

In order to validate both needle deflection models, experiments are performed in which the needle is steered toward two different target locations ($y_T = -10$ mm and $y_T = -20$ mm) by performing a single rotation. The insertion distance where rotation has to be performed x_r is determined *a priori* using both models. These distances are presented in Table I.

The resulting experimental deflection is compared with the predicted deflection using the models (see Fig. 8). The errors between experimental deflection and predicted deflection are also presented in Table I. For the first experiment ($x_T = 110$ mm, $y_T = -10$ mm), the tip error is 0.8 and 0.4 mm for the kinematics-based model and the mechanics-based model, respectively. In the second experiment ($x_T = 110$ mm, $y_T = -20$ mm), the difference in tip errors between both models is larger: 0.6 mm for the kinematics-based model and 1.7 mm for the mechanics-based model. It should be noted that the amount of needle deflection is sensitive to changes in experimental conditions. For example, it has been observed that the longevity and temperature of the soft-tissue phantom affects needle deflection. However, it is evident from these results that both models show good agreement with experimental deflection.

IV. CONTROL OF FLEXIBLE NEEDLES

The control system incorporates the kinematics-based deflection model as its accuracy is comparable with the mechanics-

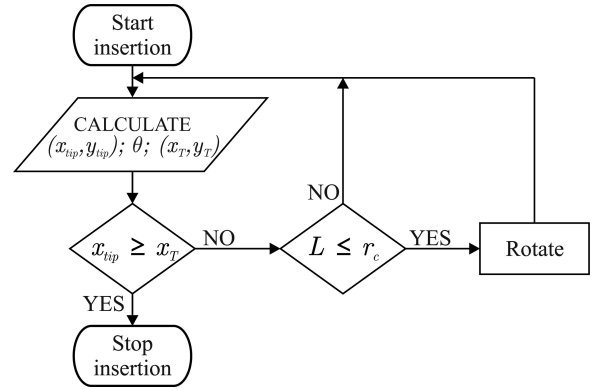


Fig. 10. Flowchart depicts the needle steering algorithm. Insertion is started and needle tip position (x_{tip}, y_{tip}) , slope θ , and target position (x_T, y_T) are determined using image processing. The insertion continues until the needle tip reaches the centre of the target ($x_{tip} \geq x_T$). Needle rotation is performed when the distance from the circle center c'_{i+1} to the target is smaller than or equal to the control radius ($L \leq r_c$).

based model. Further, the kinematics-based model is computationally efficient and suitable for real-time applications. The images used for feedback are processed to obtain the needle tip position and slope and the target position. In this section, the algorithm that is used to steer a flexible needle toward a moving target and the image processing algorithms that are used for needle and target tracking are discussed.

A. Closed-Loop Needle Steering

In the feedback control system, the needle is assumed to follow a circular path with a constant radius r_t . By rotating the needle 180° around its central axis, the needle can bend either toward the positive (upward) or negative (downward) y -direction. In Fig. 9(a), the green circle (center c'_{i+1}) represents the needle path if it rotates 180° about its axis. The distance between the target and c'_{i+1} is L . If the green circle intersects the target ($L = r_t$), the needle will rotate 180° about its axis. The location of c'_{i+1} is calculated using (2)–(9). The needle tip position is determined using image processing (see Section IV-B1).

It is important to ensure that the needle rotation does not occur late, since the needle will overshoot the target, which cannot be corrected. The control radius r_c used in the steering algorithm is chosen larger than the actual radius of curvature of the needle r_t to maintain early rotation. If the rotation occurs early, a subsequent rotation can be made to ensure that the target is reached [see Fig. 9(b)]. The flowchart that describes the steering algorithm is shown in Fig. 10. The targeting accuracy is also influenced by target motion [3]. The target moves due to tissue deformation that was caused during needle insertion, as well as physiological activities, such as respiration or blood flow [2]. In the control system, target position is tracked in real time using image processing. The target position is an input to the control system, as explained in Section IV-B.

B. Needle and Target Tracking Algorithms

Real-time needle and target tracking are required for closed-loop control of the needle (see Fig. 11). The needle tip position

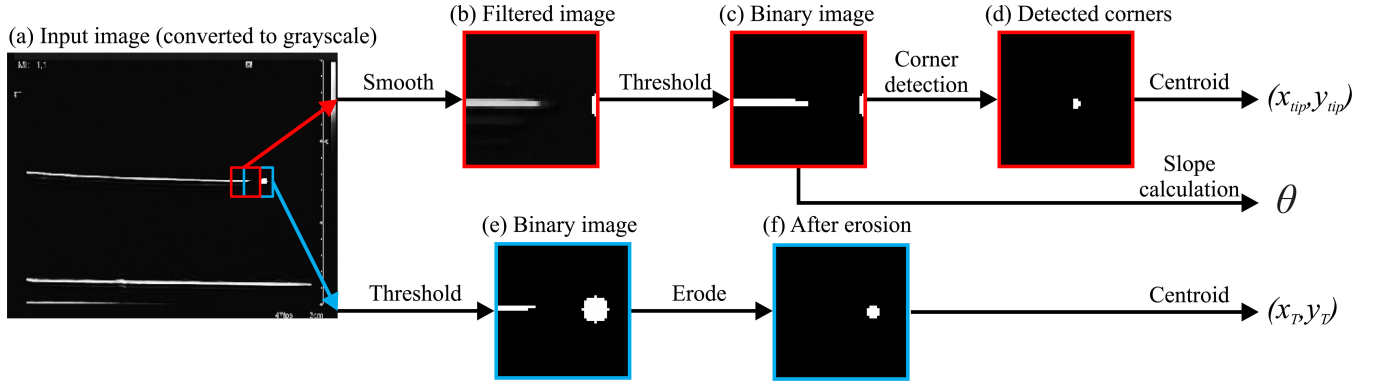


Fig. 11. Schematic shows the image processing algorithm applied to determine the needle tip position (x_{tip}, y_{tip}) and tip slope θ (red window) and target position (x_T, y_T) (blue window). (a) Input is an ultrasound image which is converted to grayscale. (b) Grayscale image is smoothed to filter out artifacts. (c) Threshold is then applied to produce a binary image. (d) Harris corner detection is applied, and then, the centroid is calculated in the output image to detect the needle tip position. (e) Binary images are acquired after performing a threshold to detect the target position. (f) Erosion is used to filter out artifacts around the target, and then, the centroid of the image is calculated to determine the target location. This algorithm is inverted after applying the threshold.

and slope can be determined using either a CCD camera or ultrasound images during insertion [see Fig. 11(b)–(d)]. The target motion is tracked in order to reduce the targeting error [see Fig. 11(e) and (f)].

1) *Needle-Tip Tracking Algorithm*: Real-time needle tip tracking is used to steer the needle tip to reach a target location. A window of 60×60 pixels is cropped from the grayscale image of the captured frame around the needle tip position [see Fig. 11(b)]. The image is smoothed to remove image artifacts and then converted to a binary image by selecting an adaptive threshold value. Adaptive thresholding is used to separate the foreground from the background with nonuniform illumination [see Fig. 11(c)]. The resulting image is then inverted, if camera images are used as the needle is darker than the background in the camera images. The Harris corner detection algorithm is applied to the binary image to determine the tip position [25]. The output of the corner detection algorithm is a binary image with a bright region at the location of the corner (needle tip) [see Fig. 11(d)]. The centroid is then calculated in the image to obtain the coordinates of the needle tip. Image moments are used to determine the centroid of the image [30], [31]. The image moments M_{ij} are defined as

$$M_{ij} := \sum_x \sum_y x^i y^j I(x, y) \quad (28)$$

where $I(x, y)$ is the pixel value at the position (x, y) in the image and x and y range over the search window. In (28), i and j are the order of moment in the directions of x and y , respectively. The centroid of the image is calculated as

$$\begin{bmatrix} x_{cen} \\ y_{cen} \end{bmatrix} = \frac{1}{M_{00}} \begin{bmatrix} M_{10} \\ M_{01} \end{bmatrix}. \quad (29)$$

The x -coordinate and y -coordinate of the image centroid are x_{cen} and y_{cen} , respectively. The needle tip slope is also required to control the needle. The tip slope θ is computed as [32]

$$\theta = \frac{1}{2} \arctan \left(\frac{2 \left(\frac{M_{11}}{M_{00}} - x_{cen} y_{cen} \right)}{\left(\frac{M_{20}}{M_{00}} - x_{cen}^2 \right) - \left(\frac{M_{02}}{M_{00}} - y_{cen}^2 \right)} \right). \quad (30)$$

2) *Target Motion Tracking*: The target position that was used in the needle steering algorithm is the measured position in each captured image frame [see Fig. 11(e) and (f)]. A window is cropped around the target. A threshold value is then applied to the image to produce a binary image in the window [see Fig. 11(e)]. The binary image is inverted when CCD camera images are used (as the target is darker than the background). Erosion is then applied on the binary image to eliminate the shapes that may affect the accuracy of target tracking [see Fig. 11(f)]. The centroid of the shape is calculated using image moments (29). The center position of the target is determined for every image frame. The distances between the position of the target in the initial frame (before needle insertion) and the following frames represent the total target displacement during needle insertion.

V. EXPERIMENTAL RESULTS

In this section, the experiments performed to validate the control system used to steer flexible needles are described. The results of the experiments are also presented in this section.

A. Experimental Plan

The aim of the experiments is to validate the tracking and steering algorithms that was used to control the needle during insertion (see Fig. 12). The kinematics-based model presented in Section III is used in the control system. The model shows accurate approximation to the actual needle deflection (see Section III-E). A Nitinol needle of $\phi 0.5$ -mm diameter is used during the experiments. The needle insertion velocity is 5 mm/s. The angular velocity during 180° needle rotation is 31.4 rad/s.

1) *Camera Image-Guided Needle Steering*: The needle is steered toward a target using CCD camera images as feedback. The needle insertion distance is 81.4–116.1 mm. The soft-tissue phantom is the same as the one used in Section III. Targets are embedded in the soft-tissue phantom.

Three experimental cases are conducted to validate the proposed control system. Each case is performed five times.

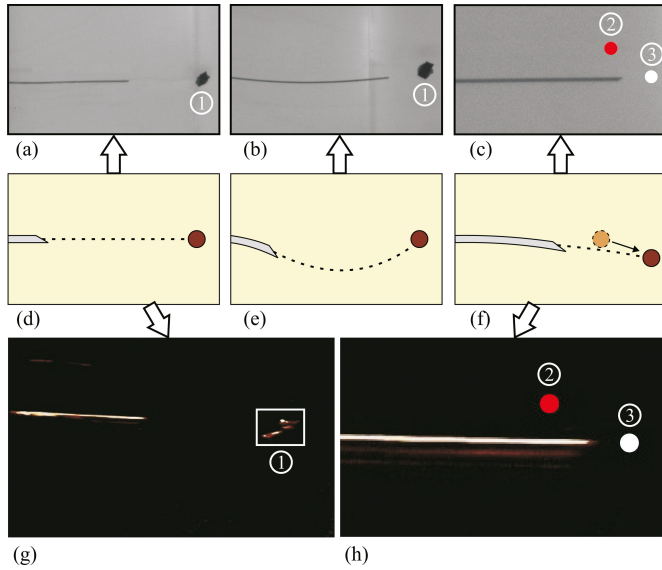


Fig. 12. Experimental cases. (a) Camera image-guidance is used to steer the needle along a straight path toward a real target ① using set points (see Case 1). (b) Camera image-guidance is used to steer the needle to follow a curved path using set points (see Case 2). (c) Camera image-guidance is used to steer the needle toward a moving virtual target where the red circle represents the initial position of the target ②, and the white circle represents the final position of the target ③. (d) Needle is inserted to reach a real target (Cases 1 and 4). (e) Needle moves along a curved path using set points (see Case 2). (f) Needle is steered toward a moving virtual target (Cases 3 and 5). (g) Ultrasound image-guidance is used to steer the needle toward a real target (see Case 4). (h) Ultrasound image-guidance is used to steer the needle toward a moving virtual target (see Case 5). See the accompanying video as supplementary material that demonstrates the experimental results.

- 1) In Case 1, the insertion point and the target are on the same horizontal line [see Fig. 12(d)]. Predefined set points are used to guide the needle to follow a straight path. This experimental case is performed to test the ability of the control system to steer a bevel-tipped needle (that naturally deflects during insertion) in a straight path.
- 2) In Case 2, the needle is again steered toward the same target position as in Case 1, but through a curved path using set points as shown in Fig. 12(e). The curved path is required in clinical applications to avoid sensitive tissues (e.g., blood vessels).
- 3) In Case 3, a moving virtual target is used to evaluate the performance of the steering algorithm [see Fig. 12(f)]. The total target displacement is chosen to be 23 mm, which is larger than the displacement measured during breast biopsy [29]. A virtual target is used to model target motion. The image processing algorithm is applied to track the virtual target position.
- 2) *Ultrasound Image-Guided Needle Steering:* Ultrasound is used for image feedback to validate the control system using a clinical imaging modality. The needle insertion distance is 29.2–30.1 mm. Two experimental cases are conducted. Each case is performed three times to estimate the targeting error as the needle visibility is affected by accuracy of aligning the needle in the ultrasound probe imaging plane [22], [23].

- 1) In Case 4, the control system is used to steer the needle toward a real target which is embedded into the soft-tissue phantom [see Fig. 12(g)].
- 2) In Case 5, the control system steers the needle to a moving virtual target (to simulate target motion). The total target displacement is 5.0 mm [see Fig. 12(h)]. The image processing algorithm is used to detect the virtual target position.

In Cases 4 and 5, silica powder is added to the ingredients of the soft-tissue phantom in order to mimic the acoustic scattering of biological tissue (14.9% gelatin powder (by weight), 1% silica gel, and 83.9% water). The elasticity is affected by the addition of silica powder to the soft-tissue phantom. The elasticity of the soft-tissue phantom is measured using an ultrasound-based technique. The speed of the shear wave propagation in the soft-tissue phantom is measured by the ARFI technique (Virtual Touch Tissue Quantification, Siemens AG Healthcare, Erlangen, Germany). The Siemens ACUSON S2000 system is used to obtain ultrasound images and to apply the ARFI technique. The linear transducer 9L4 is used to obtain the ultrasound signals for the needle steering and the shear wave propagation speed measurements. The soft-tissue phantom is assumed to be isotropic, linear elastic, and incompressible. Young's modulus E is calculated as [39]

$$G = v_s^2 \rho \quad (31)$$

where G , v_s , and ρ are the shear modulus, shear wave propagation speed, and density of the soft-tissue phantom, respectively. The density is calculated using the mass and volume of the soft-tissue phantom. Young's modulus E calculated by

$$E = 2G(1 + \gamma) \quad (32)$$

where γ is Poisson's ratio which is assumed to be 0.495. The ARFI technique is not valid for transparent soft-tissue phantoms (without silica powder). The calculated elastic modulus of the soft-tissue phantom (after adding silica powder) is 57.69 ± 3.71 kPa. The elasticity of the soft-tissue phantom sample was independently verified using the uniaxial compression test, and is found to be 63.7 ± 5.9 kPa. Silica powder increases the elastic modulus of the soft-tissue phantom so the calculated radius of curvature r_t is expected to decrease [8]. This will not affect the targeting accuracy of the control algorithm, as r_t remains less than r_c .

B. Results

The pixel resolution of the CCD camera and ultrasound images are 1024×768 and 720×576 pixels, respectively. The frame rate of the captured images is 25 frames/s. The experimental results in Section III are used to estimate the needle radius of curvature r_t . In all the experimental cases, the control radius r_c is chosen to be equal to the maximum r_t measured in order to compensate for inaccuracies that might occur while performing the experiments. The five experimental cases are described in Fig. 12. The number of needle rotations and targeting errors during insertion are tabulated in Table II.

In Cases 1, 2, and 4, the diameter of the target is 4.0 mm (real target), and in Cases 3 and 5, the target diameter is 1.7 mm

TABLE II
NEEDLE INSERTION DISTANCE, NUMBER OF ROTATIONS, AND TARGETING ERROR FOR THE VARIOUS EXPERIMENTAL CASES DURING NEEDLE STEERING ARE PRESENTED

Case	<i>int</i> (mm)	<i>rot</i>	<i>e_x</i> (mm)	<i>σ_x</i> (mm)	<i>e_y</i> (mm)	<i>σ_y</i> (mm)	<i>e</i> (mm)	<i>σ</i> (mm)
1	86.7	19	0.38	0.16	0.30	0.25	0.55	0.04
2	105.0	6	0.45	0.10	0.34	0.17	0.59	0.04
3	81.7	2	0.13	0.08	0.23	0.17	0.35	0.15
4	29.2	3	0.36	0.30	0.11	0.05	0.39	0.28
5	30.1	2	0.29	0.24	0.25	0.12	0.42	0.18

The mean needle insertion distance and number of rotations for each case are *int* and *rot*, respectively. The mean targeting error in *x* and *y* directions are *e_x* and *e_y*, respectively. The standard deviation in *x* and *y* directions are *σ_x* and *σ_y*, respectively. The mean and standard deviation of the absolute targeting error are *e* and *σ*, respectively.

(moving virtual target). The targeting error is measured by calculating the distance between the center of the target and the needle tip position in the last frame. The maximum absolute targeting error is 0.59 mm [see Case 2: Fig. 12(b) and (e)]. In ultrasound image-guided experiments (see Cases 4 and 5), the absolute targeting errors are 0.39 and 0.42 mm, respectively. In Cases 3 and 5, in which moving virtual targets are used, the targeting errors are 0.35 and 0.42 mm, respectively. The results show that the needle reaches the target for all cases. It is observed that the targeting error occurs mainly when the needle overshoots the target. Overshooting can occur due to time delay in the control system. This can be improved by reducing the loop time of the control system.

VI. DISCUSSION

This study combines needle deflection models and image-guided techniques to accurately steer bevel-tipped flexible needles to a moving target. Two different models have been presented to predict the deflection of a needle undergoing multiple bends. Image processing is used to determine the needle and target positions in a camera and ultrasound images. Experiments are performed to evaluate the targeting accuracy of the proposed control system.

A. Conclusion

The needle deflection models presented include a modified kinematics-based unicycle model that accounts for needle cut angle, and a mechanics-based model that incorporates needle-tissue interactions. Both models predict deflections for multiple bends. The maximum needle deflection errors at the tip are 0.8 and 1.7 mm for the kinematics-based and mechanics-based models, respectively. This indicates that both models are in good agreement with experimental results. The real-time image-guided control system uses the kinematics-based model to predict when needle rotation has to be performed for steering. Image processing is used to determine needle tip position and slope and target position during needle insertion for feedback control. The steering algorithm accounts for target motion to improve targeting accuracy. The proposed real-time needle and target tracking algorithms are applicable to both camera and ultrasound images. The tracking algorithms can also be applied to other clinical imaging modalities. Experiments using ultrasound image-guided control demonstrate that the control system is able to steer the needle to a moving target with mean error of 0.42 mm. The smallest tumor that can be detected using ultra-

sound images has a diameter of around 2.0 mm [40]. This implies that with the achieved accuracy of the steering algorithm, we can target the smallest detected tumors using ultrasound images.

B. Future Work

The control system will be used to steer flexible needles in biological tissue. The effect of image artifacts that might appear while steering through biological tissue using ultrasound images needs to be investigated. Further, the effect of needle rotations on tissue damage should be quantified. Both (mechanics-based and kinematics-based) models need to be modified to predict needle deflection in a 3-D space. The tracking and the steering algorithm will be extended to three dimensions to enable the needle to reach out-of-plane targets. The control system will include path planning algorithms to select the optimal path that the needle can follow to reach a target.

REFERENCES

- [1] A. M. Okamura, C. Simone, and M. D. O'Leary, "Force modeling for needle insertion into soft tissue," *IEEE Trans. Biomed. Eng.*, vol. 51, no. 10, pp. 1707–1716, Oct. 2004.
- [2] J. op den Buijs, M. Abayazid, C. L. de Korte, and S. Misra, "Target motion predictions for pre-operative planning during needle-based interventions," in *Proc. IEEE Int. Conf. Eng. Med. Biol. Soc.*, Boston, MA, Sep. 2011, pp. 5380–5385.
- [3] H. Tadayyon, A. Lasso, S. Gill, A. Kaushal, P. Guion, and G. Fichtinger, "Target motion compensation in MRI-guided prostate biopsy with static images," in *Proc. IEEE Int. Conf. Eng. Med. Biol. Soc.*, Buenos Aires, Argentina, Sep. 2010, pp. 5416–5419.
- [4] A. Grant and J. Neuberger, "Guidelines on the use of liver biopsy in clinical practice," *J. Gastroenterology Hepatol.*, vol. 45, no. Suppl. IV, pp. IV1–IV11, 1999.
- [5] D. Glezman and M. Shoham, "Image-guided robotic flexible needle steering," *IEEE Trans. Robot.*, vol. 23, no. 3, pp. 459–467, Jun. 2007.
- [6] R. J. Webster, J. S. Kim, N. J. Cowan, G. S. Chirikjian, and A. M. Okamura, "Nonholonomic modeling of needle steering," *Int. J. Robot. Res.*, vol. 25, no. 5/6, pp. 509–525, 2006.
- [7] R. J. Roesthuis, M. Abayazid, and S. Misra, "Mechanics-based model for predicting in-plane needle deflection with multiple bends," in *Proc. IEEE Int. Conf. Biomed. Robot. Biomechatronics*, Rome, Italy, Jun. 2012, pp. 69–74.
- [8] Y. R. J. van Veen, A. Jayha, and S. Misra, "Macroscopic and microscopic observations of needle insertion into gels," *Proc. Inst. Mech. Eng. Part H: J. Eng. Med.*, vol. 226, pp. 441–449, Jun. 2012.
- [9] R. J. Roesthuis, Y. R. J. van Veen, A. Jayha, and S. Misra, "Mechanics of needle-tissue interaction," in *Proc. IEEE Int. Conf. Intell. Robot. Syst.*, San Francisco, CA, Sep. 2011, pp. 2557–2563.
- [10] S. P. DiMaio and S. E. Salcudean, "Needle steering and model-based trajectory planning," in *Proc. Int. Conf. Med. Imag. Comput. Comput.-Assist. Intervention*, Montréal, QC, Canada, Nov. 2003, vol. 2878, pp. 33–40.
- [11] H. Kataoka, T. Washio, K. Chinzei, K. Mizuhara, C. Simone, and A. M. Okamura, "Measurement of the tip and friction force acting on

- a needle during penetration,” in *Proc. Int. Conf. Med. Imag. Comput. Comput.-Assist. Intervention*, Tokyo, Japan, Sep. 2002, pp. 216–223.
- [12] R. Alterovitz, A. Lim, K. Goldberg, G. S. Chirikjian, and A. M. Okamura, “Steering flexible needles under Markov motion uncertainty,” in *Proc. IEEE Int. Conf. Intell. Robot. Syst.*, Edmonton, AB, Canada, Aug. 2005, pp. 1570–1575.
- [13] N. Abolhassani and R. V. Patel, “Deflection of a flexible needle during insertion into soft tissue,” in *Proc. IEEE Int. Conf. Eng. Med. Biol. Soc.*, New York, Sep. 2006, pp. 3858–3861.
- [14] N. A. Wood, K. Shahrou, M. C. Ost, and C. N. Riviere, “Needle steering system using duty-cycled rotation for percutaneous kidney access,” in *Proc. IEEE Int. Conf. Eng. Med. Biol. Soc.*, Buenos Aires, Argentina, Sep. 2010, pp. 5432–5435.
- [15] N. J. Cowan, K. Goldberg, G. S. Chirikjian, G. Fichtinger, K. B. Reed, V. Kallem, W. Park, S. Misra, and A. M. Okamura, “Robotic needle steering: Design, modeling, planning, and image guidance,” in *Surgical Robotics*. New York: Springer-Verlag, 2011, pp. 557–582.
- [16] S.-Y. Ko, L. Frasson, and F. R. y Baena, “Closed-loop planar motion control of a steerable probe with a “programmable bevel” inspired by nature,” *IEEE Trans. Robot.*, vol. 27, no. 5, pp. 970–983, Oct. 2011.
- [17] A. Haddadi and K. Hashtrudi-Zaad, “Development of a dynamic model for bevel-tip flexible needle insertion into soft tissues,” in *Proc. IEEE Int. Conf. Eng. Med. Biol. Soc.*, Boston, MA, Sep. 2011, pp. 7478–7482.
- [18] C. Chui, S. Teoh, C. Ong, J. Anderson, and I. Sakuma, “Integrative modeling of liver organ for simulation of flexible needle insertion,” in *Proc. 9th Int. Conf. Control Autom. Robot. Vis.*, Singapore, Dec. 2006, pp. 1–6.
- [19] J. A. Engh, G. Podnar, S. Y. Khoo, and C. N. Riviere, “Flexible needle steering system for percutaneous access to deep zones of the brain,” in *Proc. IEEE Annu. Northeast Bioeng. Conf.*, Easton, PA, Apr. 2006, pp. 103–104.
- [20] H. Kataoka, T. Washio, M. Audette, and K. Mizuhara, “A model for relations between needle deflection, force, and thickness on needle penetration,” in *Proc. Int. Conf. Med. Imag. Comput. Comput.-Assist. Intervention*, vol. 2208, Utrecht, The Netherlands, Oct. 2001, pp. 966–974.
- [21] S. Misra, K. B. Reed, B. W. Schafer, K. T. Ramesh, and A. M. Okamura, “Mechanics of flexible needles robotically steered through soft tissue,” *Int. J. Robot. Res.*, vol. 29, no. 13, pp. 1640–1660, 2010.
- [22] Z. Neubach and M. Shoham, “Ultrasound-guided robot for flexible needle steering,” *IEEE Trans. Biomed. Eng.*, vol. 57, no. 4, pp. 799–805, Apr. 2010.
- [23] I. Schafhalter-Zoppoth, C. E. McCulloch, and A. T. Gray, “Ultrasound visibility of needles used for regional nerve block: An in vitro study,” *Regional Anesthesia Pain Med.*, vol. 29, no. 5, pp. 480–488, 2004.
- [24] S. H. Okazawa, R. Ebrahimi, J. Chuang, R. N. Rohling, and S. E. Salcudean, “Methods for segmenting curved needles in ultrasound images,” *Med. Imag. Anal.*, vol. 10, no. 3, pp. 330–342, 2006.
- [25] C. Harris and M. Stephens, “A combined corner and edge detector,” in *Proc. 4th Alvey Vis. Conf.*, Manchester, U.K., Aug./Sep. 1988, vol. 15, pp. 147–151.
- [26] N. Abolhassani, R. V. Patel, and M. Moallem, “Needle insertion into soft tissue: A survey,” *Med. Eng. Phys.*, vol. 29, no. 4, pp. 413–431, 2007.
- [27] N. D. Glossop, K. Cleary, L. Kull, and F. Banovac, “Needle tracking using the aurora magnetic position sensor,” in *Proc. Comput. Assist. Orthopaedic Surg.*, Santa Fe, NM, Jun. 2002, pp. 90–92.
- [28] H. Su, M. Zervas, G. A. Cole, C. Furlong, and G. S. Fischer, “Real-time MRI-guided needle placement robot with integrated fiber optic force sensing,” in *Proc. IEEE Int. Conf. Robot. Autom.*, Shanghai, China, May 2011, pp. 1583–1588.
- [29] E. E. Deurloo, K. G. Gilhuijs, L. J. S. Kool, and S. H. Muller, “Displacement of breast tissue and needle deviations during stereotactic procedures,” *Investigative Radiol.*, vol. 36, no. 6, pp. 347–353, 2001.
- [30] M.-K. Hu, “Visual pattern recognition by moment invariants,” *IRE Trans. Inf. Theory*, vol. 8, pp. 179–187, Feb. 1962.
- [31] M. R. Teague, “Image analysis via the general theory of moments*,” *J. Opt. Soc. Amer.*, vol. 70, no. 8, pp. 920–930, 1980.
- [32] *Open Source Computer Vision Library, Reference Manual*, 1st ed., Intel Corp., Santa Clara, CA, 2000.
- [33] E. S. Melerski, *Design Analysis Beams Circular Plates and Cylindrical Tanks on Elastic Foundations*. New York: Taylor & Francis, 2000.
- [34] O. Bauchau and J. Craig, *Structural Analysis*. New York: Springer-Verlag, 2009.
- [35] J. Gere and S. Timoshenko, *Mechanics of Materials*. London, U.K.: Stanley Thornes, 1999.
- [36] A. Gefen and B. Dilmoney, “Mechanics of the normal woman’s breast,” *Technol. Health Care*, vol. 15, no. 4, pp. 259–271, 2007.
- [37] S. DiMaio and S. Salcudean, “Needle insertion modelling and simulation,” in *Proc. IEEE Int. Conf. Robot. Autom.*, Washington, DC, May 2002, pp. 2098–2105.
- [38] V. Pratt, “Direct least-squares fitting of algebraic surfaces,” *ACM Comput. Graph.*, vol. 21, no. 4, pp. 145–152, 1987.
- [39] M. L. Palmeri, M. H. Wang, J. J. Dahl, K. D. Frinkley, and K. R. Nightingale, “Quantifying hepatic shear modulus in vivo using acoustic radiation force,” *Ultrasound Med. Biol.*, vol. 34, no. 4, pp. 546–558, 2008.
- [40] Stjoeshealth.org. (2011). *The importance of mammography* [Online]. Available: <http://www.stjoeshealth.org/>



Momen Abayazid (S’12) received the B.Sc. degree in systems and biomedical engineering from Cairo University, Giza, Egypt, in 2007 and the M.Sc. degree in biomedical instrumentation from the Delft University of Technology, Delft, The Netherlands, in 2010. He is currently working toward the Doctoral degree with the Control Engineering Group, the University of Twente, Enschede, The Netherlands.

His research interests include medical robotics and biomedical engineering.



Roy J. Roesthuis (S’11) received the B.Sc. degree in electrical engineering and the M.Sc. degree in mechatronics, both from the University of Twente, Enschede, The Netherlands, in 2009 and 2011, respectively, where he is currently working toward the Doctoral degree with the Control Engineering Group.

His research interests include robotics for medical procedures.



Rob Reilink (S’08) received the B.Sc. degree in 2007 and the M.Sc. (Hons.) degree in 2008 from the University of Twente, Enschede, The Netherlands, both in electrical engineering, where he is currently working toward the Doctoral degree with the Control Engineering Group.

His research interests include image processing, visual servoing, and haptics.



Sarthak Misra (S’05–M’10) received the Master’s degree from McGill University, Montreal, QC, Canada, and the Doctoral degree from the Johns Hopkins University, Baltimore, MD, both in mechanical engineering.

He is currently an Associate Professor of control engineering with the MIRA Institute for Biomedical Technology and Technical Medicine, University of Twente, Enschede The Netherlands. Prior to commencing his studies at Johns Hopkins, he was a Dynamics and Controls Analyst on the International Space Station Program for three years. His research interests include biomechanics and robotics.

Dr. Misra received the 2010 Netherlands Organization for Scientific Research VENI Award. He is the Associate Editor of the IEEE Robotics and Automation Society Conference Editorial Board.